ASSESSMENT OF QUALITY OF ELASTICITY IMAGES OBTAINED USING DIFFERENT ULTRASOUND SYSTEMS

An Undergraduate Research Scholars Thesis

by

SAMANTHA J. MORGANTI

Submitted to the LAUNCH: Undergraduate Research office at
Texas A&M University
in partial fulfillment of requirements for the designation as an

UNDERGRADUATE RESEARCH SCHOLAR

Approved by
Faculty Research Advisor: Dr. Raffaella Righetti

May 2022

Major: Electrical Engineering

RESEARCH COMPLIANCE CERTIFICATION

Research activities involving the use of human subjects, vertebrate animals, and/or biohazards must be reviewed and approved by the appropriate Texas A&M University regulatory research committee (i.e., IRB, IACUC, IBC) before the activity can commence. This requirement applies to activities conducted at Texas A&M and to activities conducted at non-Texas A&M facilities or institutions. In both cases, students are responsible for working with the relevant Texas A&M research compliance program to ensure and document that all Texas A&M compliance obligations are met before the study begins.

I, Samantha J. Morganti, certify that all research compliance requirements related to this Undergraduate Research Scholars thesis have been addressed with my Research Faculty Advisor prior to the collection of any data used in this final thesis submission.

This project did not require approval from the Texas A&M University Research Compliance & Biosafety office.

TABLE OF CONTENTS

ABSTRACT

Assessment of Quality of Elasticity Images Obtained Using Different Ultrasound Systems

Samantha J. Morganti
Department of Electrical and Computer Engineering
Texas A&M University

Research Faculty Advisor: Dr. Rafaella Righetti
Department of Electrical and Computer Engineering
Texas A&M University

Elastography is an ultrasonic imaging modality, which is useful in gaining new information about tissues and diagnosing diseases. Increasing the quality of an image allows for more accurate information to be gained from the image and better interpret the experimental results. Theoretical and simulation work has been done to determine how the parameters of an ultrasound system affect the quality of elasticity images but limited experimental validation has been performed so far. This study investigates the quality of elasticity images obtainable by using ultrasound systems with different specifications. Image quality is analyzed in terms of contrast-to-noise ratio, signal-to-noise ratio, and spatial resolution. These quality factors in elastography depend on mechanical parameters (such as applied strain and boundary conditions), acoustic parameters (such as transducer center frequency, bandwidth, etc.), and signal-processing parameters (such as window length and window separation for cross-correlation based strain estimation methods). Two ultrasound systems operating with different frequencies and bandwidths will be used, and the analysis will be carried out using theoretical and simulation software as well as experimental data. Theoretical and simulation results demonstrate that the

system with higher center frequency and larger bandwidth produce elastographic images with higher quality. Experimentally, the attainable improvement is expected to be lower than the one predicted by theory and simulations. This project builds on prior theoretical research with new experimental data to demonstrate that ultrasound systems with increased ultrasonic capabilities (in terms of frequency, bandwidth, beamwidth, etc.) produce elasticity images with higher quality. As these systems are used for identification of elastographic markers in tissues such as cancers, understanding their quality limitations using a systematic study will be useful to understand and interpret future pre-clinical and clinical data.

ACKNOWLEDGEMENTS

Contributors

I would like to thank my faculty advisor, Dr. Raffaella Righetti for her guidance and support throughout the course of this research. I also would like to thank my graduate mentor, Sharmin Majumder, for her care and dedication to my success.

Thanks also go to my friends and colleagues and the department faculty and staff for making my time at Texas A&M University a great experience.

Finally, thanks to my mother and father for their encouragement and support.

Funding Sources

Undergraduate research was not supported by funding.

NOMENCLATURE

CNR	Contrast-to-Noise Ratio
HT	Hilbert Transform
LSQE	Least-Squares Estimation
PR	Poisson’s ratio
RF	Radiofrequency
SNR	Signal-to-Noise Ratio
TDE	Time Delay Estimation
US	Ultrasound
YM	Young’s modulus

1. INTRODUCTION

Ultrasound is defined as acoustic waves with a frequency above 20 kHz. Biomedical applications use ultrasound ranging between 2 to 18 MHz [1]. In medical applications, ultrasound is used to image blood flow, view various organs within the body, diagnose diseases, and obtain information about tissues. Among the reasons why ultrasound imaging is popular in medicine is because it is safe, non-invasive, and radiation-free.

An ultrasound system uses a transducer to transmit ultrasound into tissue and to receive the reflected sound. The received radiofrequency (RF) data is processed by the system based on the speed of sound and time taken by the echo signals to come back to the transducer. Echoes are created from the ultrasound waves either reflected or scattered from the tissue boundaries. The received data can be further processed by the system, or a computer user, to generate different imaging modalities such as B-mode (Sonography), Doppler, elasticity imaging etc., which can provide information of the imaged tissues.

B-mode images are the typical gray-scale images, also referred to as “sonograms”. They are cross-sectional 2D images in which tissues and organs are represented [2]. “B” stands for ‘Brightness’ as these grayscale images are composed of points of varying brightness, whose intensity is dependent on the strength or amplitude of the received echo signal. B-mode are generated from the RF signals by demodulation, which, mathematically, can be performed using the Hilbert transform. Log compression is also typically applied to the Hilbert transformed data for better visualization [2]. B-mode images cannot give information about tissue stiffness or fluid velocity.

Imaging tissue elastic parameters (Elastography) for diagnosis of a disease has become increasingly important due it its non-invasive nature and its ability to complement standard diagnostic modalities [3]. Elastography is an imaging modality that uses ultrasonic data obtained from compressed soft tissue to form images of the local strains, also referred to as "elastograms" [4]. Elastograms can be used to detect the presence and severity of various diseases based on changes in the mechanical properties of the tissue. Pathological changes of tissues have been correlated to tissue stiffness. For example, certain lesions may not possess sonographic contrast that would make them ultrasonically detectable [5], however the difference in stiffness could make them detectable using elastography. The performance of elastography depends on a number of parameters, which include: the tissue biomechanical properties, the algorithm used to estimate the tissue displacements and strains and the physical properties of the ultrasound system used to collect the ultrasonic data [3, 4]. Theoretical and simulation works have been performed to predict the quality obtainable using different ultrasonic systems. However, limited experimental validation has been performed so far. While ultrasonic parameters such as the ultrasonic frequency, bandwidth, pitch, and beamwidth are expected to affect the image quality of elastograms, the actual attainable improvement could be lower than the one predicted by the theoretical studies [6].

The quality of the ultrasound images is typically quantified using signal-to-noise ratio (SNR), contrast-to-noise ratio (CNR), and spatial resolution [4]. These quality attributes depend on mechanical parameters (such as applied strain and boundary conditions), acoustic parameters (such as transducer center frequency, bandwidth, beamwidth, and pitch), and signal- processing parameters (such as window length and window separation) [3, 4]. With respect to the physical parameters of the ultrasound system, it has been shown theoretically that SNR, CNR, and spatial

resolution all improve with larger bandwidths and higher center frequencies [3, 4]. Image quality parameters are also shown to increase when using narrower beamwidths and smaller pitches [3]. More specifically, bandwidth and center frequency affect the quality of axial strain elastograms while beamwidth and pitch affect the quality of lateral strain elastograms [4, 7].

In this study, the image quality of elastograms, and B-mode images obtained using two different ultrasound (US) systems are statistically compared. One system is manufactured by Verasonics (Vantage 256, Verasonics Inc, Kirkland, WA) and the other is a SonixTouch US system (Analogic Corporation, Peabody, MA, USA). This comparative analysis is done; a) theoretically, based on strain filter theory [6]; b) in terms of B-mode images using both a dedicated ultrasound simulation software (Field II) and experimental data; and c) in terms of elastograms generated by both simulations (convolution model) and experiments. The quality of the various images was quantified using SNR, CNR, and spatial resolution. T-test was used to statistically determine if there is a significant difference between the two systems for each quality parameter. My results show that Vantage 256 US system has a better SNR than SonixTouch US system. However, I found no statistically significant difference between the two systems for CNR and spatial resolution at a 95% confidence level.

The thesis is organized as follows. In chapter 2, the methods used to conduct the study are presented. In chapter 3, the results of the experiments, and simulations are presented and discussed. Finally, the conclusion of the study is presented in chapter 4.

2. METHODS

This study uses the ultrasound system parameters of Vantage 256 US system (referred as "system A" in this thesis), and SonixTouch US system (referred as 'system B" in this thesis) to quantify the image quality of B-mode and elasticity images through simulations, experiments, and theory.

System A uses a linear array transducer that is 2.5 cm long and has 256 elements. The transducer operates at a center frequency of 15 MHz and has 80% bandwidth (at -6 dB) and 1 mm beamwidth (at the focus). System B uses a linear array transducer that is 3.8 cm long and has 128 elements. The transducer operates at a center frequency of 6.6 MHz and has 50% bandwidth (at - 6 dB) and 1 mm beamwidth (at the focus).

The procedural flow of data analysis in this study is shown in Figure 2.1. Image quality parameters, SNR, CNR, and spatial resolution, are computed from elastography and B-mode images generated by simulations and experiments. Strain filter theory [6] is implemented to compare the simulation and experimental results with the theoretical predictions. The parameters obtained experimentally are expected to be somewhat similar to the simulation parameters and the strain filter theory. A t-test is done to statistical analyze if the image quality of the two systems is significantly different. The methodology for generating B-mode images and elastograms by simulations and experiments is detailed in the following subsections.

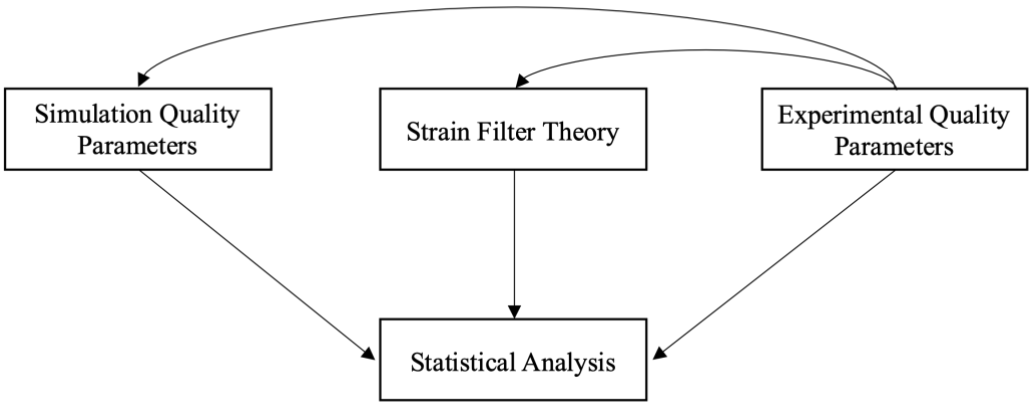

Figure 2.1: Flowchart of project design

2.1 B-mode Imaging Modality

2.1.1 Generating B-mode Images from RF Data

To obtain B-mode images from the RF data simulated or collected from the US systems, a sequence of signal processing steps is applied, shown in Figure 2.2. First, the Hilbert Transform (HT) is applied to the RF signal. HT is an envelope detection technique used to demodulate the RF signal [8]. The envelope of the signal is the magnitude of the analytic signal, calculated from the HT [8]. The envelope is then mapped non-linearly using log compression, which improved the dynamic range of the displayed images.

Figure 2.2: Sequence of steps used to obtain b-mode images from RF data.

2.1.2 B-mode Image Simulation

Radiofrequency (RF) data was simulated using the Field II Ultrasound Simulation Program [9]. Field II is an available software program used to simulate ultrasound transducer fields and ultrasound imaging using linear acoustics [9]. The program allows the simulation of

non-stationarity of the pressure beam and can calculate the emitted and pulse-echo fields for a large number of different transducers [9]. The program environment allows to input transducer parameters (center frequency, sampling frequency, number of elements, etc.), and phantom parameters (phantom size, inclusion size, and phantom contrast to background) to simulate RF data. In this study, 1 uniform (without inclusion) and 5 non-uniform (with inclusion) phantoms were simulated. Among the non-uniform phantoms, 3 phantoms were simulated with inclusion stiffer than the background, and the other 2 phantoms are with inclusion less stiff than the background. This was done by increasing the amplitude of the scatters to be a multiple or a fraction of the background. All simulated phantoms had a width of 50 mm, a depth of 10 mm, and a height of 60 mm. The inclusions were cylindrical with a diameter of 6 mm and a depth of 10 mm. These parameters for the simulated ultrasound systems matched the ultrasound parameters of two experimental systems (system A and system B). After simulating RF data by Field II software, B-mode images were generated using the methods described in *2.1.1*.

2.1.3 B-mode Phantom Experiment

Two non-uniform 3D phantoms with cylindrical inclusions were created for experimental imaging [10]. The background of each phantom was made of 5% gelatin and 3% agar content. The inclusion of one phantom was made of 8% gelatin and 5% agar content and the second phantom was made of 10% gelatin and 8% agar. A cubic mold of $5x5.5x5$ cm^3 was used to make the phantoms with cylindrical inclusions. The cylinder was 1 cm in diameter.

To make each phantom, the gelatin and agar were mixed in an appropriate amount of boiling deionized water while being manually stirred [10]. The mixture was then poured into the mold and refrigerated at 7°C for 12 hours [10]. The background was then checked for solidification and the inclusion mixture was poured into the cylindrical cavity left in the mold

[10]. The phantom was then refrigerated at 7°C for an additional 12 hours [10]. After the phantom was completely solidified, it was removed from the mold for imaging.

Each phantom was imaged with ultrasound system A and B to obtain RF data for B-mode images. While imaging, cold water was used between the phantom and the probe surface to avoid the presence of air gaps.

2.2 Elastography Imaging Modality

2.2.1 Generating Elastograms from RF Data

The sequence of steps used in this thesis to calculate elastograms from RF data is shown in Figure 2.3.

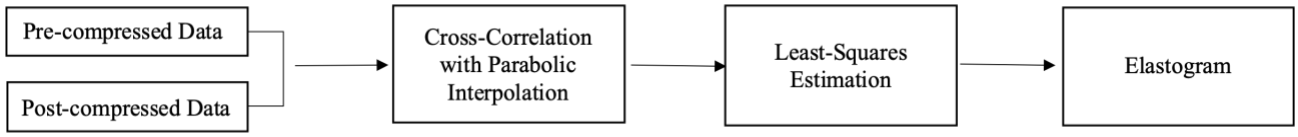

Figure 2.3: Sequence of steps used to obtain elastograms from RF data.

Pre- and post-compression RF data is required to compute elastograms. Pre-compression RF data is collected before applying compression on the tissue whereas post-compression RF data is collected after compression. The ultrasound systems discussed in this thesis can take a series of temporal frames of RF data during the compression over a course of time. From the RF temporal data, we can choose pre- and post-compression frames by comparing them by taking cross correlation of corresponding scan lines.

From pre- and post- compressed RF data, displacement maps are generated. To compute displacement, in this study, I used a cross-correlation technique [2]. This technique utilizes time delay estimation (TDE) to estimate local tissue displacements. Time delays are estimated from the peaks of the cross-correlation function [5]. This involves segmenting the RF data in temporal windows and then computing the cross-correlation between congruent pairs of pre- and post-

compression windows. The position of the peak of the cross-correlation windows is the displacement between the two windows. Parabolic interpolation is used to estimate sub-sample displacements. The window length is usually chosen as 10 wavelengths, with a 20% window overlap. It has been shown that the choice of the window length and overlap affects the quality of the elastograms [3, 4].

From the displacement maps, strain elastograms are obtained using the least-squares estimation (LSQE) [11]. While a simple gradient technique can be used to compute strain elastograms, [11] in this study, LSQE technique is used to reduce the noise and improve SNR [11] of the elastograms. The LSQE technique aims at fiting a piecewise linear curve to the data that minimizes the squared error between the data and the model [11]. Given a small kernel with N points, the least square equation is given by *Eq*. 2.1, where *a* is the estimation of the strain at the middle of the kernel, *A* is an Nx2 matrix where the first row is the depth position of the kernel and the second is a row of ones, and *u* contains the displacement data.

$$\begin{bmatrix} a \\ b \end{bmatrix} = A^T [AA^T]^{-1} u \qquad \textit{(Eq. 2.1)}$$

2.2.2 Elastogram Simulation

To simulate elasticity images, it is first necessary to use a mechanical simulation software, which allows to determine the ideal displacements occurring into the phantom use to the application of an external compression. These displacements depend on the geometry of the phantom, the mechanical properties of the phantom and the boundary conditions. Subsequently, these displacements are used as input to an in-house ultrasound simulation software [12], which generates the simulated pre- and post-compression simulated RF data. Therefore, elastography simulations were done using two simulation software in two steps as follows.

- Step I: ABAQUS, a commercial FE simulation software [12] was used to generate 3D simulated displacement maps of the phantom subjected to the external compression.
- Step II: A convolution-based US simulation software was used to generate RF data using the ideal displacement map collected from ABAQUS.

In step I, ABAQUS was used to create the displacements of samples under boundary conditions mimicking real elastography experiments [12]. The samples were compressed from the top and the bottom was kept static, to replicate the physical experiment. Seven uniform samples were simulated for the study. The percent strain of the samples varies from 0.5% to 10% strain. Two non-uniform samples were simulated for the study. Sample A had a Young's modulus (YM) of 50 for the inclusion and 32.78 for the background, and a Poisson's ratio (PR) of 0.45 for the inclusion and 0.47 for the background. Sample C had a YM of 97.02 for the inclusion and 32.78 for the background, and a PR of 0.45 for the inclusion and 0.47 for the background. Displacement data was obtained from the software. This displacement data was used in step II to simulate ultrasound RF data. Table 2.1 summarizes the properties of the uniform simulated samples used in this study. Table 2.2 summarizes the properties of the non-uniform simulated samples used in this study.

Table 2.1: Parameters used to simulate 5 uniform samples for strain image analysis.

Phantom	Percent Strain	Gaussian Noise
a	0.5%	40 dB
b	1%	40 dB
c	2%	10 dB
d	2%	20 dB

e	2%	40 dB
f	5%	40 dB
g	10%	40 dB

Table 2.2: Parameters used to simulate 2 non-uniform samples for strain image analysis.

Phantom	Young's Modulus		Poisson's Ratio	
	Inclusion	Background	Inclusion	Background
A	50	32.78	0.45	0.47
B	97.02	32.78	0.45	0.47

In step II, convolution-based US simulation software was used to simulate pre and post compressed RF data from the displacement map [12]. To generate the simulated RF data, ultrasonic parameters of system A and system B were used. The simulated ultrasound transducer of system A had 256 elements, a 15 MHz center frequency, and 80% fractional bandwidth at −6 dB. The transducer's beamwidth was assumed to be dependent on the wavelength and to be approximately 1 mm at 15 MHz. The simulated ultrasound transducer of system B had 128 elements, a 6.6 MHz center frequency, and 50% fractional bandwidth at −6 dB. The transducer's beamwidth was assumed to be dependent on the wavelength and to be approximately 1 mm at 6.6 MHz. The sampling frequency was set at 40 MHz and Gaussian noise was added to set the SNR at 10, 20, and 40 dB.

After simulating pre and post compressed RF signals for two US systems, ultrasound simulated displacement was computed by using the method explained in *2.2.1*. Displacement was computed by taking the cross-correlation with a window size of 2 mm and a window overlap

of 0.4 mm. To compute the elasticity image, least squares estimation (LSQE) was applied to the displacement image.

2.2.3 Elastogram Phantom Experiment

One non-uniform 3D phantom with a cylindrical inclusion was created for experimental imaging. The background of the phantom was made of 5% gelatin and 3% agar content. The inclusion of the phantom was made of 8% gelatin and 5% agar content. Figure 2.4 below shows an image of the first phantom in the axial position. A cubic mold of $5x5.5x5$ cm^3 was used to make the phantoms with cylindrical inclusions. The cylinder was 1 cm in diameter.

Figure 2.4: Experimental phantom in the axial view

The phantom was imaged with ultrasound system A and B to obtain pre- and post-compression RF data to create elasticity images. The experimental set-up to obtain data elasticity images is shown in Figure 2.5. The transducer was attached to the compression plate on top of the phantom. The compression plate was used to apply equal pressure to the top of the phantom and reduce lateral movement when applying pressure. While imaging, a very light pre-

compression force was applied to ensure the probe was completely touching the phantom when capturing the pre-compression data frames.

Figure 2.5: Elasticity imaging experimental set-up

2.3 Quality Parameters

Quality of elasticity and B-mode images was quantified using three quality parameters: signal-to-noise ratio (SNR), contrast-to-noise ratio (CNR), and spatial resolution. These three quality parameters are discussed in the following subsections.

2.3.1 Signal-to-Noise Ratio (SNR)

SNR is computed by the equation shown in *Eq. 2.2* [13], where μ_s and σ_s are the mean and standard deviation of a homogenous phantom. To obtain SNR from an image, the mean and standard deviation of a rectangular portion of the image were used. As noise increases in the image, the standard deviation will also increase, leading to a smaller SNR value. This indicates that larger values of SNR represent images of higher image quality.

$$SNR = \frac{\mu_s}{\sigma_s} \qquad \textit{(Eq. 2.2)}$$

2.3.2 Contrast-to-Noise Ratio (CNR)

CNR is shown in *Eq. 2.3*, where μ_i is the mean of the inclusion, μ_o is the mean of the background, and σ_i and σ_o are the corresponding variances of a non-homogenous phantom [13]. CNR and contrast differ because image contrast depends only on the ratio of means, while CNR also depends on the standard deviation of the noise [13]. To obtain CNR from an image, the mean and standard deviation of a rectangular portion of the inclusion and the mean and standard deviation of a rectangular portion of the background were used. As noise increases in the image, the standard deviation will also increase, leading to a smaller CNR value. This indicates that larger values of CNR represent images of higher image quality.

$$CNR = \frac{|\mu_i - \mu_o|}{\sqrt{\sigma_i^2 + \sigma_o^2}} \qquad \textit{(Eq. 2.3)}$$

2.3.3 Spatial Resolution

Spatial resolution is typically defined as the measure of the smallest distance between two closely spaced objects that can be detected by the system. By this definition, the image with a smaller value of spatial resolution is assumed to have higher quality. One possible way to assess spatial resolution limitations of a system is to measure the full width half maximum (FWHM) of the inclusion in an image. This is described as the width of the inclusion as half of its maximum amplitude. This is the method that was used in this study. The profile of an inclusion is depicted in Figure 2.6 with the FWHM labeled. The ideal case, shown in blue, defines a vertical inclusion rise, while the non-ideal case, shown in black, defines a gradual inclusion rise. As the inclusion becomes more ideal, the FWHM will widen increasing the value. Due to how spatial resolution is measured, the image with a higher value of FWHM has higher quality.

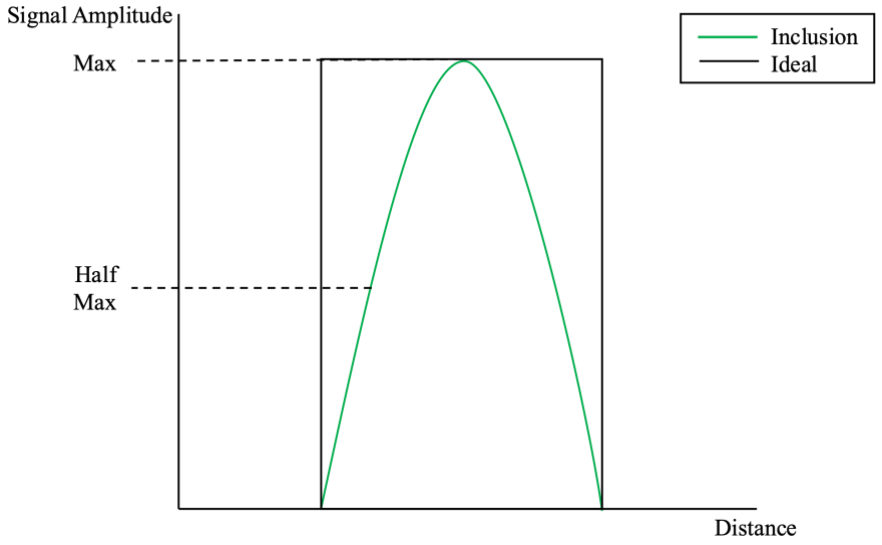

Figure 2.6: Profile of an ideal and non-ideal inclusion. The full-width half maximum is defined for the non-ideal inclusion.

2.4 Strain Filter Theory

The strain filter theoretical framework predicts the upper bound of the elastographic signal-to-noise ratio (SNR_e) based on the properties of the ultrasound system and the signal processing parameters used to compute the displacements and strains [6]. To obtain the upper bound of the SNR_e, the total tissue strain (s_t) and the lower bound on the strain estimation standard deviation (σ_{ZZLB}) are substituted into *Eq. 2.4*.

$$SNR_e^{UB} = \frac{s_t}{\sigma_{ZZLB}} \qquad \textit{(Eq. 2.4)}$$

According to the strain filter theory, accurate estimation of the strain is possible only within the Cramer-Rao lower bound (CRLB) region [4]. The strain estimation variance used is shown in Equation 2.5, where the minimum variance is given by the CRLB (σ_{CRLB}) as detailed in Eq. 2.6 [4].

$$\sigma_{ZZLB}^2 = \frac{2\sigma_{CRLB}^2}{T\Delta t} \quad \textit{(Eq. 2.5)}$$

$$\sigma_{CRLB}^2 = \frac{3}{2\pi^2(B^3 + 12Bf_o^2)}\left[\frac{1}{\rho^2}\left(1 + \frac{1}{SNR^2}\right)^2 - 1\right] \quad \textit{(Eq. 2.6)}$$

The parameters are represented as follows: T is the temporal window size, Δt is the temporal window overlap, B is the bandwidth, f_o is the center frequency, ρ is the correlation coefficient (*Eq. 2.7*), and SNR is the sonographic SNR. The additional parameters in the equations are: $f = \frac{2f_o}{c}$ (where c is the speed of sound in tissue = 1.54 mm/Ms) is the spatial frequency in cycles/mm, $\sigma_u = \frac{B^2}{\pi c}$ is the standard deviation of the Gaussian envelope in cycles/mm, α represents the axial compression, and β represents the corresponding lateral compression.

$$\rho = \frac{2\sqrt{\alpha\beta}}{\sqrt{2(\alpha^2+1)(\beta^2+1)}} e^{-\frac{1}{2}\left(\frac{f}{\sigma_u}\right)^2 \frac{(\alpha-1)^2}{\alpha^2+1}} \quad \textit{(Eq. 2.7)}$$

The strain filter is computed using the ultrasound parameters for each system for 0.5, 1, 2, 5, and 10 percent strain. The parameters used for system A are as follows: a temporal window size of 1.3 μs, a temporal window overlap of 0.26 μs, a center frequency of 15 MHz, a transducer bandwidth 12 MHz, and a sonographic SNR of 40 dB. The parameters used for system B are as follows: a temporal window size of 2.6 μs, a temporal window overlap of 0.52 μs, a center frequency of 6.6 MHz, a transducer bandwidth of 3.3 MHz, and a sonographic SNR of 40 dB. System A is expected to have a higher elastographic SNR than system B, because of the increase in center frequency and bandwidth, and the decrease in the window size and window overlap.

3. RESULTS AND DISCUSSION

3.1 B-mode Results

3.1.1 Simulation Results

Figure 3.1 shows example simulated B-mode images for the system A (a, c) and System B (b, d) for a uniform and non-uniform phantom. The inclusion of the phantom is stiffer than the background. The images show the system A to have finer speckle, indicating system A has a higher SNR. The contrast of each inclusion compared to the background is expected to be the same, as depicted below, due to the influence of the material properties on the CNR measurement. The inclusion appears larger for system A. In addition, the simulated speckle appears to be finer for System A than for System B, where the speckle is coarser. This is a consequence of the higher frequency and bandwidth of system A. The same trends were seen for the b-mode images of the phantom experiment.

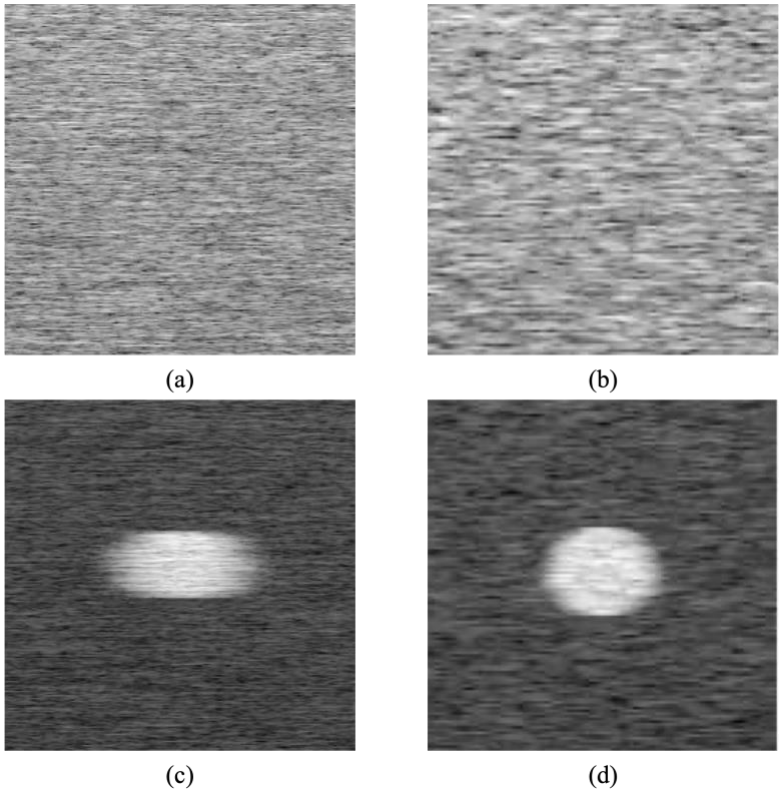

Figure 3.1: (a) Example of a simulated b-mode image of a uniform phantom using system A's parameters to simulate. (b) Example of a simulated b-mode image of a uniform phantom using system B's parameters to simulate. (c) Example of a simulated b-mode image of a non-uniform phantom using system A's parameters to simulate. (d) Example of a simulated b-mode image of a non-uniform phantom using system B's parameters to simulate.

3.1.2 Phantom Experiment Results

Figure 3.2 below shows example experimental b-mode images for the system A (a) and System B (b) for the same non-uniform phantom. The images show the system A to have finer speckle, indicating system A has a higher SNR and qualitative resolution. The contrast of each inclusion compared to the background appears to be the same, as depicted below, presumably due to the influence of the material properties on the CNR measurement. The phantom appears larger for system A because the dimension of the US probe from system A is smaller than system B.

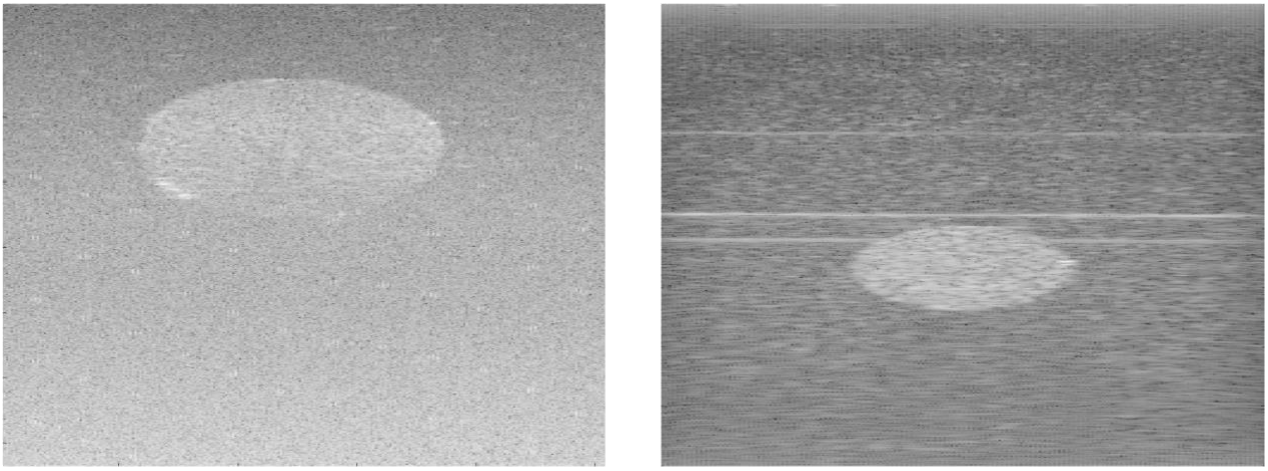

Figure 3.2: (a) Example of experimental b-mode image obtained using system A. (b) Example of experimental b-mode image obtained using system B.

3.1.3 Statistical Analysis

Figures 3.3 compares the measured CNR of simulated b-mode images for 5 different non-uniform phantoms. Based on the data, the CNR is not statistically different between the two systems.

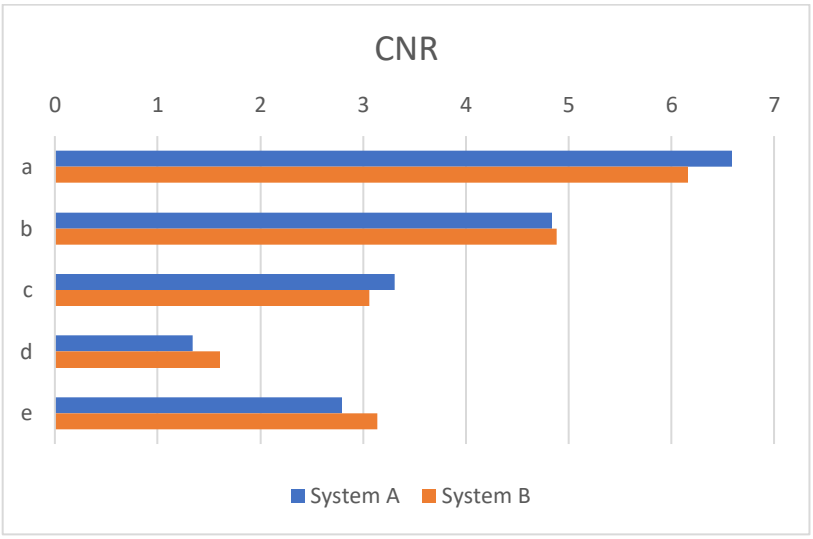

Figure 3.3: Measured CNR for simulated b-mode images of phantoms a through e

Figure 3.4 compares the measured spatial resolution of simulated b-mode images for 5 different non-uniform phantoms. The spatial resolution is statistically different between the two systems. Based on the data, System A has a better spatial resolution.

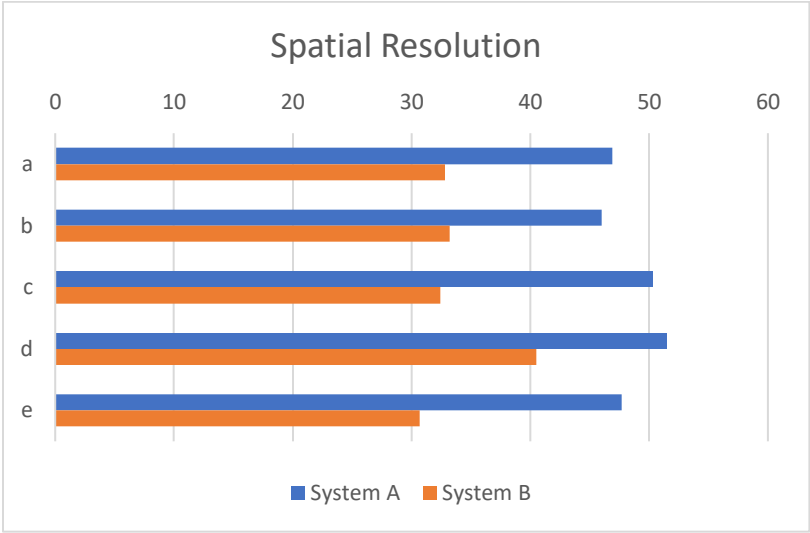

Figure 3.4: Measured spatial resolution for simulated b-mode images of phantoms a through e

Figure 3.5 compares the measured SNR of simulated b-mode images for 1 uniform phantom. Based on the data, the SNR is not statistically different. The small difference in SNR of the two images comes from the speckle size, which is finer in the system A's image.

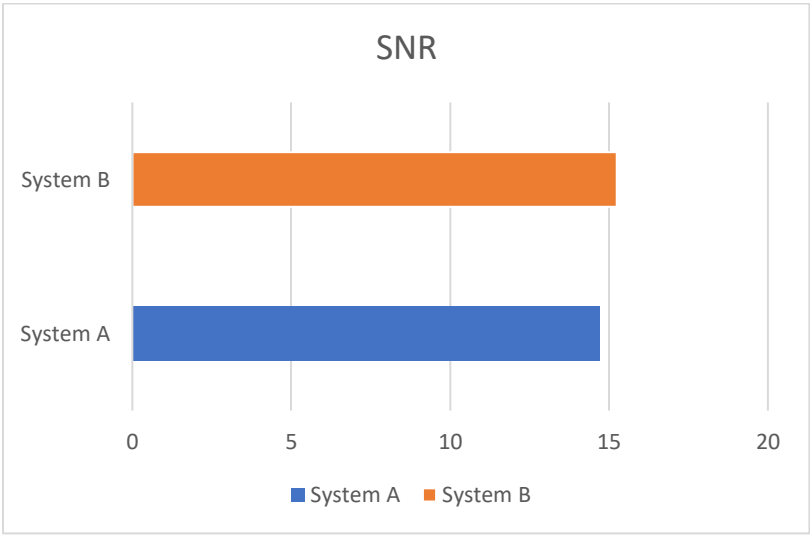

Figure 3.5: Measured SNR for simulated b-mode images of phantom f

Figures 3.6 compares the measured CNR of experimental b-mode images for 2 different phantoms. Based on the data, the CNR is not statistically different between the two systems (at a 95% confidence level).

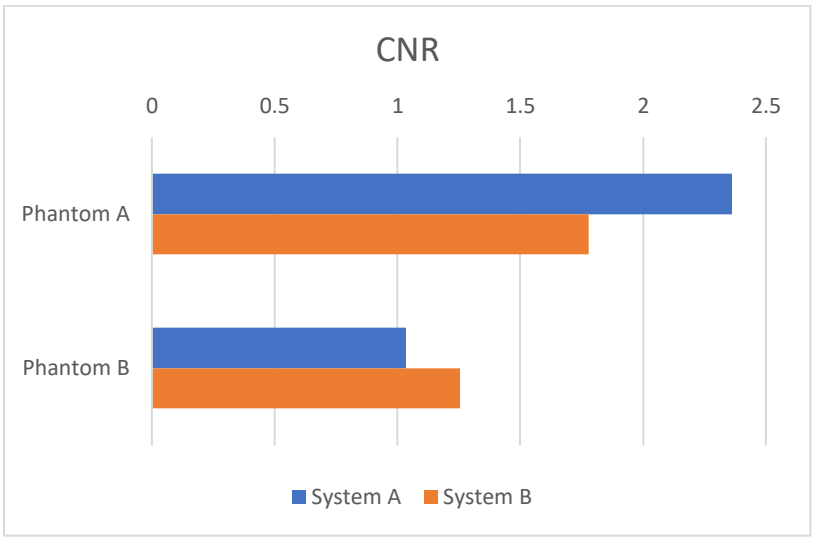

Figure 3.6: Measured CNR for experimental b-mode images of 2 phantoms.

Figure 3.7 compares the measured spatial resolution of experimental b-mode images for 2 different phantoms. Based on the data, the spatial resolution is not statistically different between the two systems.

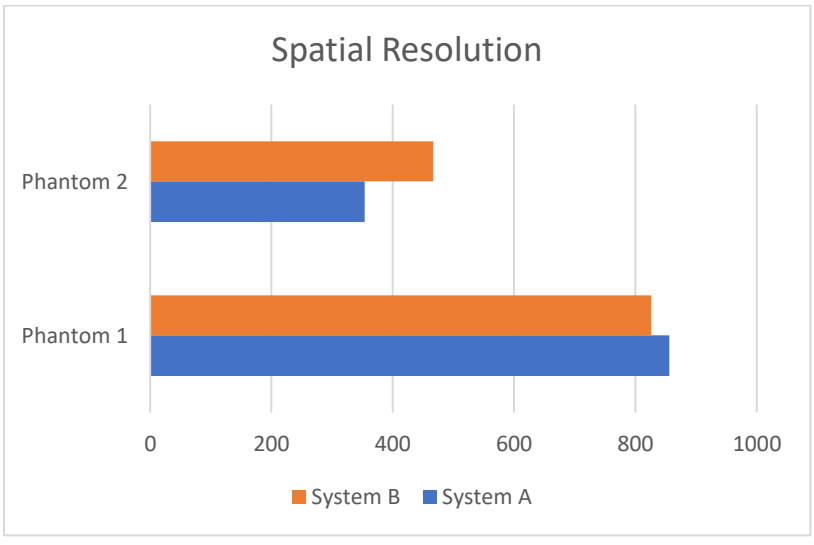

Figure 3.7: Measured spatial resolution for experimental b-mode images of 2 phantoms.

Figure 3.8 compares the measured SNR of experimental b-mode images for 2 different phantoms. Based on the data, the SNR is statistically different; System A has better SNR.

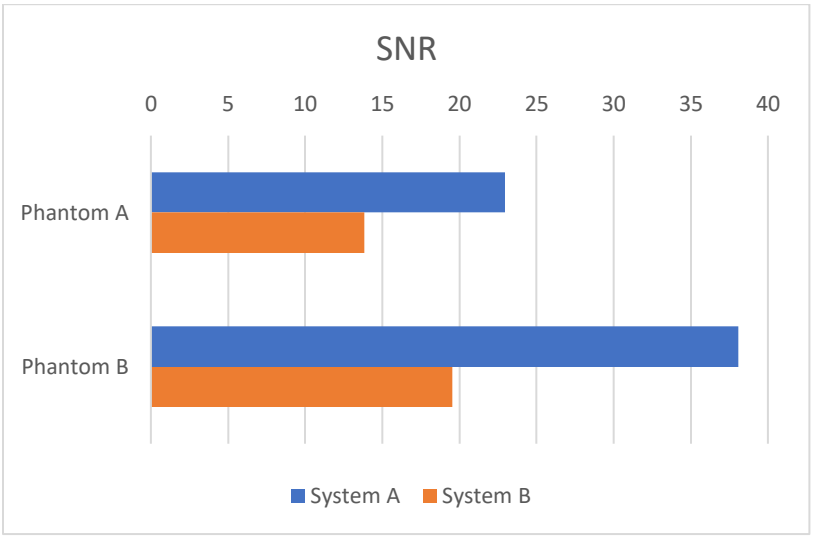

Figure 3.8: Measured SNR for experimental b-mode images of 2 phantoms.

Overall, system A produces b-mode images with higher SNR quality. The difference between system A and system B b-mode image quality in terms of CNR and spatial resolution is, in general, not significant.

3.2 Elastography Results

3.2.1 Simulation Results

Figure 3.9 below shows examples of simulated strain images for the system A (a, c) and System B (b, d) for a uniform and non-uniform phantom. Qualitatively, the image simulated using system A's parameters has less noise in the inclusion, as well as in the background of the phantom, indicating system A has a higher SNR. The inclusion/background does not seem to change, as depicted below. Still qualitatively, the margins of the inclusion appear to be better defined in the elastogram for system A. Thus, system A may produce elastograms with better spatial resolution. However, it is unclear if the difference in spatial resolution between the two

systems is statistically significant. Similar trends were observed for the strain images obtained using the experimental phantom data.

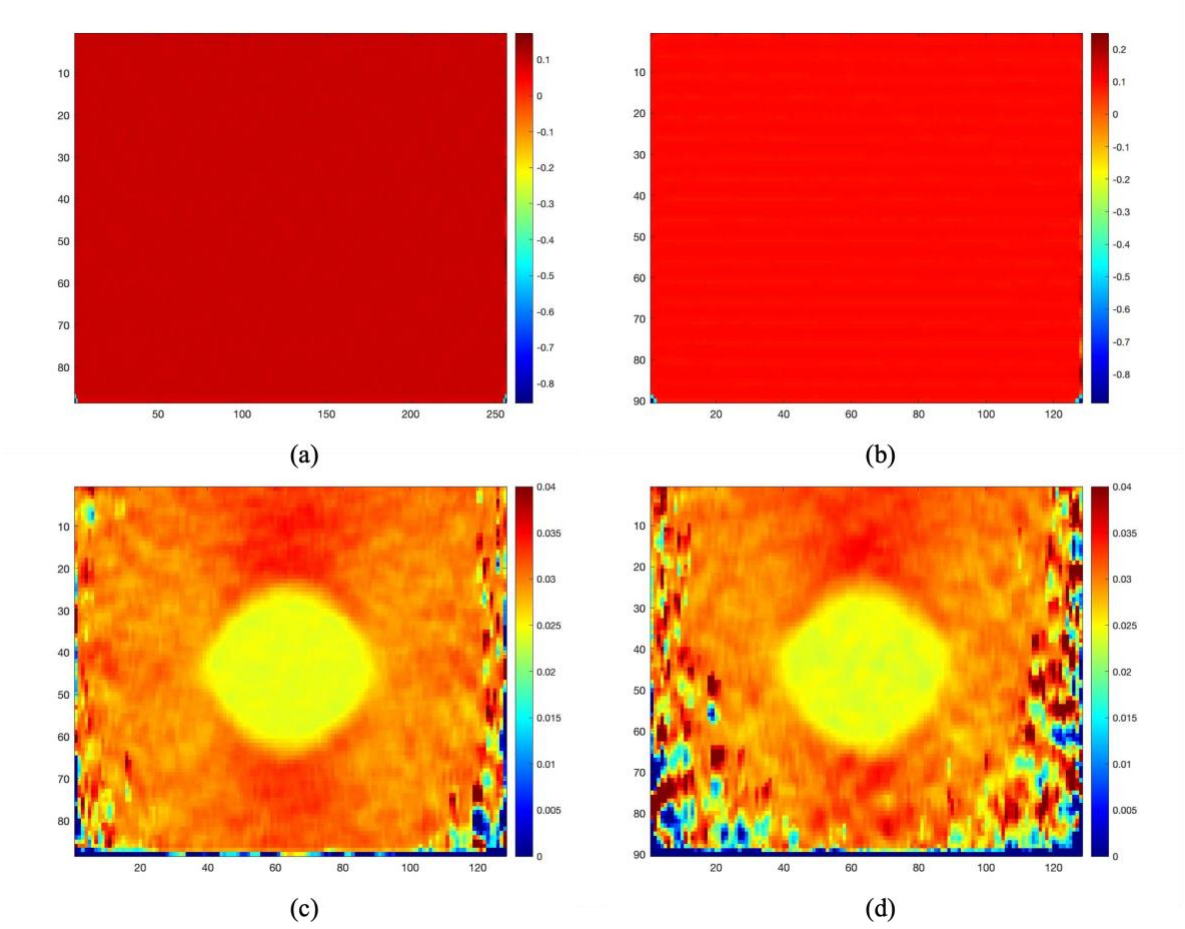

Figure 3.9: (a) Example of a simulated strain image of a uniform phantom using system A's parameters to simulate. (b) Example of a simulated strain image of a uniform phantom using system B's parameters to simulate. (c) Example of a simulated strain image of a non-uniform phantom using system A's parameters to simulate. (d) Example of a simulated strain image of a non-uniform phantom using system B's parameters to simulate.

3.2.2 Phantom Experiment Results

Figure 3.10 below shows examples of experimental strain images for the system A (a) and System B (b) for the same non-uniform phantom. Qualitatively, the images show system A to have finer texture, indicating system A may have a higher SNR. The contrast of each inclusion compared to the background does not seem to change, as depicted below. The inclusion appears

slightly better defined in the elastograms obtained from system A, suggesting that system A may have better spatial resolution.

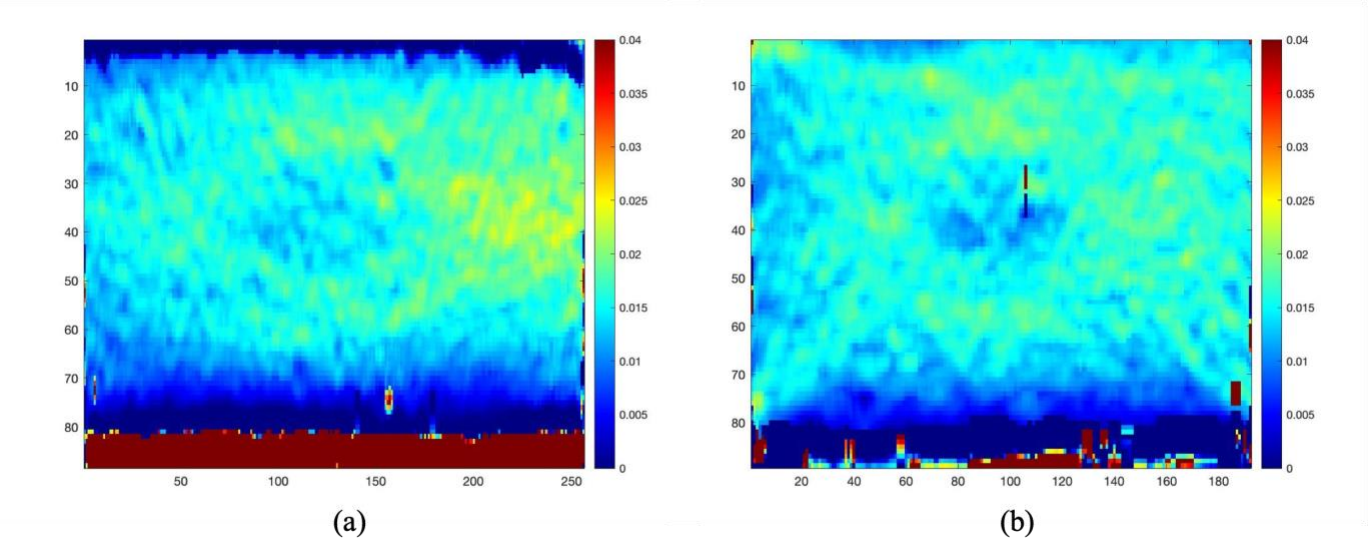

Figure 3.10: (a) Example of experimental strain image obtained using system A. (b) Example of experimental strain image obtained using system B.

3.2.3 Statistical Analysis

Figures 3.11 compares the measured CNR of simulated strain images for 2 different non-uniform phantoms. The CNR is not statistically different between the two systems.

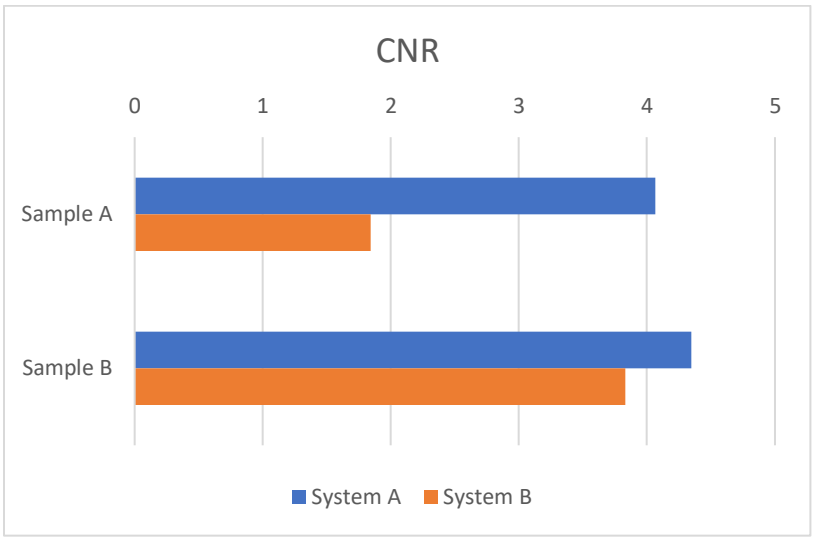

Figure 3.11: Measured CNR for simulated strain images of samples A and B

Figure 3.12 compares the measured spatial resolution of simulated b-mode images for 2 different non-uniform phantoms. Based on the data, the spatial resolution is not statistically different between the two systems.

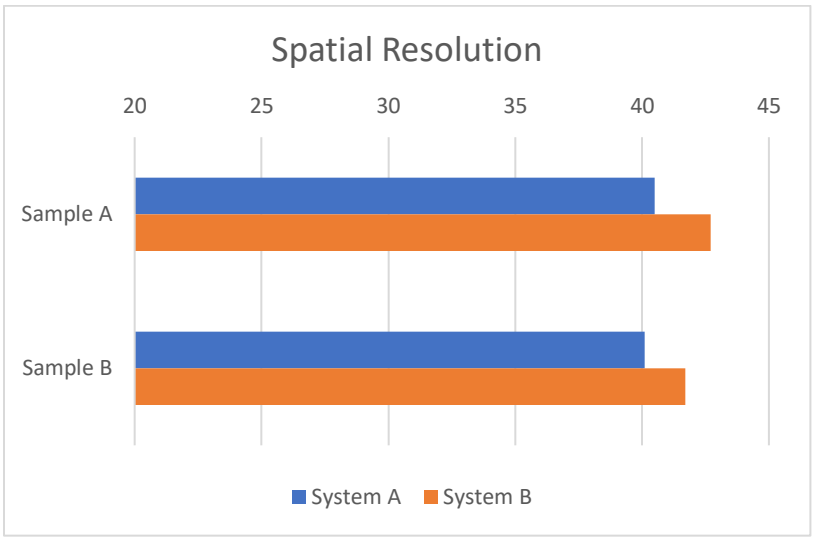

Figure 3.12: Measured spatial resolution for simulated strain images of samples A and B

Figure 3.13 compares the measured SNR of simulated strain images for 7 uniform phantoms. Based on the data, System A has higher SNR than system B.

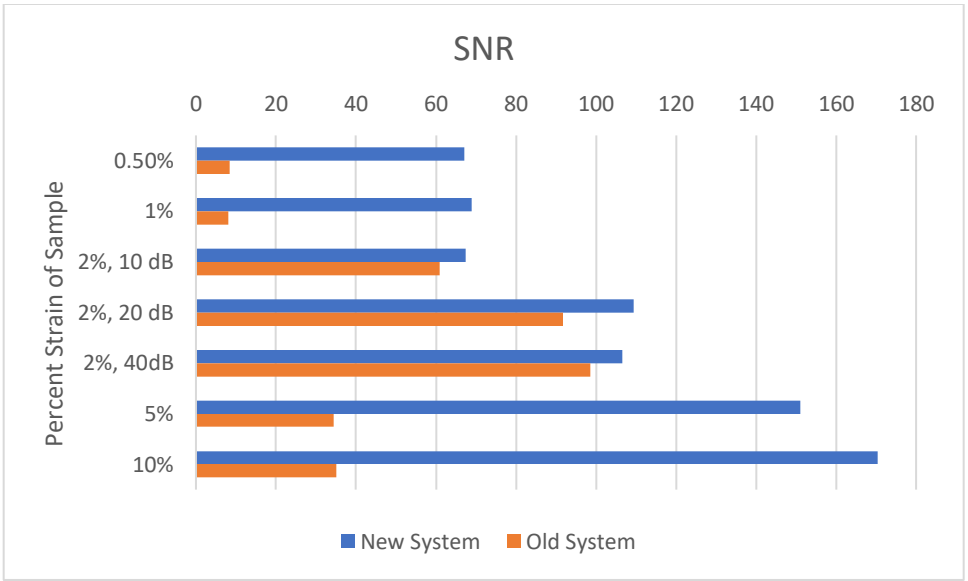

Figure 3.13: Measured SNR for simulated strain images of 7 uniform samples.

Figures 3.14 compares the measured CNR of experimental strain images for a phantom. The CNR is not statistically different between the two systems.

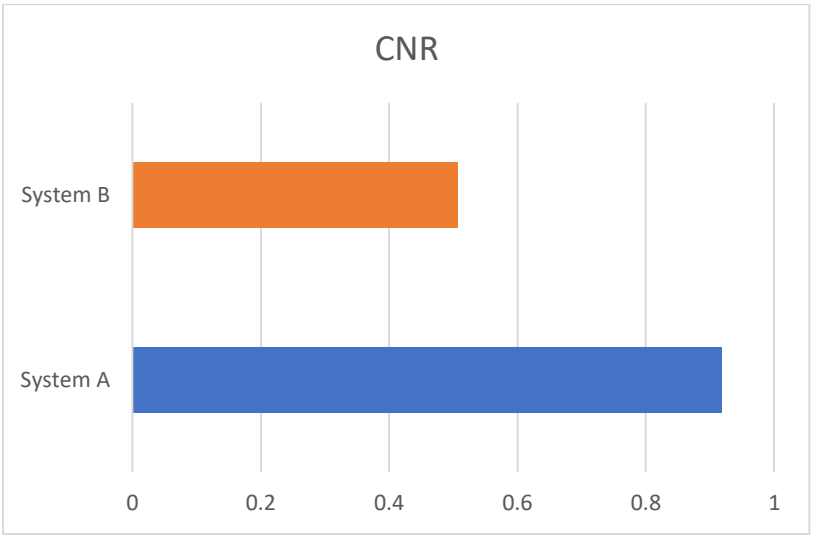

Figure 3.14: Measured CNR for experimental strain images of 2 phantoms.

Figure 3.15 compares the measured spatial resolution of experimental strain images for a phantom. Based on the data, the spatial resolution is not statistically different between the two systems.

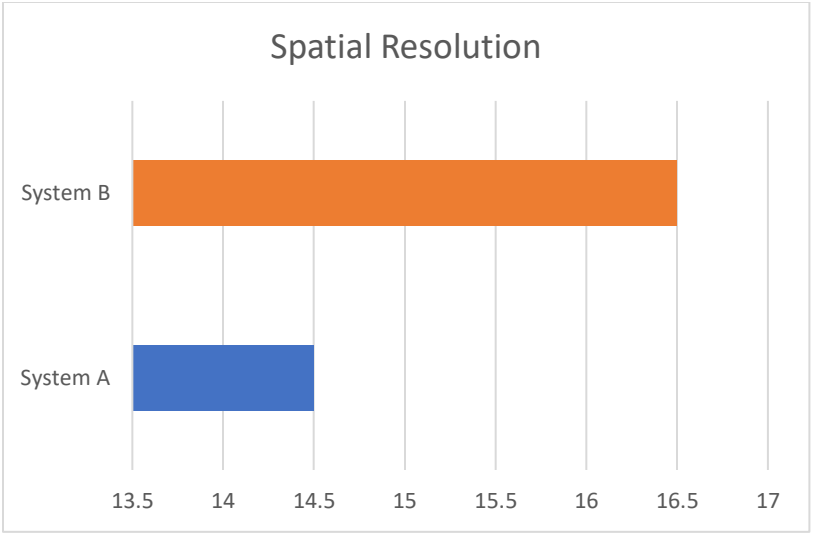

Figure 3.15: Measured spatial resolution experimental strain images of 2 phantoms.

Figure 3.16 compares the measured SNR of experimental strain images for a phantom. Based on the data, System A has better SNR.

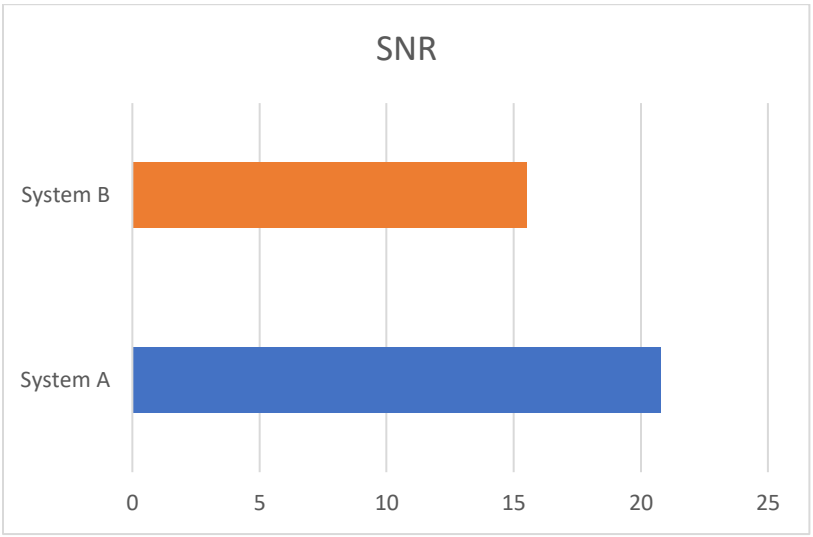

Figure 3.16: Measured SNR for experimental strain images of 2 phantoms.

Overall, system A produces strain images with higher SNR quality. The difference between system A and system B strain image quality in terms of CNR and spatial resolution is not significant.

3.3 Strain Filter Theory

Figure 3.17 below compares the theoretical elastographic SNR for system A and system B using the strain filter theory. The calculations were done with an equal window size of 2 mm. As the percent strain increases, the SNR of system A increases at a quicker rate than system B. Based on this plot, system A has higher image quality, theoretically.

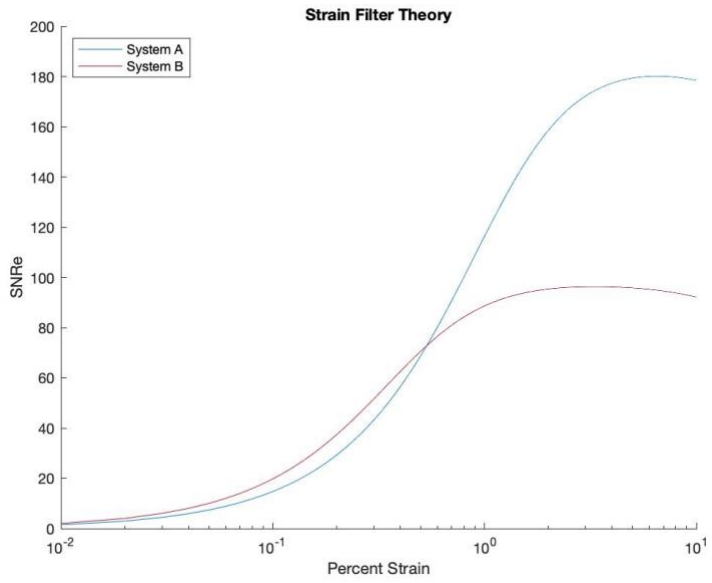

Figure 3.17: Strain Filter Theory for system A and system B using 2 mm as the window size.

4. CONCLUSION

In this study, the quality of B-mode and elastography imaged generated by two ultrasound systems with different ultrasonic parameters were compared in terms of SNR, CNR, and spatial resolution. The two ultrasound imaging modalities, b-mode imaging and elastography, were compared using simulations, experiments, and the strain filter theory. Overall, the system with higher frequency and bandwidth produced higher quality images in terms of SNR. While, qualitatively, images from system A appear to have better CNR and spatial resolution, this study found no statistically significant difference in image quality in terms of CNR and spatial resolution (at a 95% confidence level).

REFERENCES

[1] A. Carovac, F. Smajlovic, and D. Junuzovic, "Application of ultrasound in medicine," *Acta Inform Med,* vol. 19, no. 3, pp. 168-71, Sep 2011, doi: 10.5455/aim.2011.19.168-171.

[2] D. A. Christensen, *Ultrasonic bioinstrumentation*. New York: Wiley (in English), 1988.

[3] T. Varghese, J. Ophir, E. Konofagou, F. Kallel, and R. Righetti, "Tradeoffs in elastographic imaging," *Ultrason Imaging,* vol. 23, no. 4, pp. 216-48, Oct 2001, doi: 10.1177/016173460102300402.

[4] S. Srinivasan, R. Righetti, and J. Ophir, "Trade-offs between the axial resolution and the signal-to-noise ratio in elastography," (in eng), *Ultrasound Med Biol,* vol. 29, no. 6, pp. 847-66, Jun 2003, doi: 10.1016/s0301-5629(03)00037-1.

[5] J. Ophir *et al.*, "Elastography: Imaging the elastic properties of soft tissues with ultrasound," (in eng), *J Med Ultrason (2001),* vol. 29, no. 4, p. 155, Dec 2002, doi: 10.1007/bf02480847.

[6] T. Varghese and J. Ophir, "A theoretical framework for performance characterization of elastography: the strain filter," *IEEE Trans Ultrason Ferroelectr Freq Control,* vol. 44, no. 1, pp. 164-72, 1997, doi: 10.1109/58.585212.

[7] R. Righetti, S. Srinivasan, and J. Ophir, "Lateral resolution in elastography," (in eng), *Ultrasound Med Biol,* vol. 29, no. 5, pp. 695-704, May 2003, doi: 10.1016/s0301-5629(03)00028-0.

[8] C. Wachinger, T. Klein, and N. Navab, "The 2D analytic signal for envelope detection and feature extraction on ultrasound images," *Med Image Anal,* vol. 16, no. 6, pp. 1073-84, Aug 2012, doi: 10.1016/j.media.2012.05.001.

[9] J. A. Jensen. "Field II ultrasound simulation program." https://field-ii.dk/ (accessed 2021).

[10] F. Kallel, J. Prihoda Cd Fau - Ophir, and J. Ophir, "Contrast-transfer efficiency for continuously varying tissue moduli: simulation and phantom validation," (in eng), no. 0301-5629 (Print).

[11] F. Kallel and J. Ophir, "A least-squares strain estimator for elastography," *Ultrason Imaging*, vol. 19, no. 3, pp. 195-208, Jul 1997, doi: 10.1177/016173469701900303.

[12] M. T. Islam, A. Chaudhry, and R. Righetti, "A Robust Method to Estimate the Time Constant of Elastographic Parameters," *IEEE Trans Med Imaging*, vol. 38, no. 6, pp. 1358-1370, Jun 2019, doi: 10.1109/TMI.2019.2894782.

[13] M. T. Islam, A. Chaudhry, S. Tang, E. Tasciotti, and R. Righetti, "A New Method for Estimating the Effective Poisson's Ratio in Ultrasound Poroelastography," *IEEE Trans Med Imaging*, vol. 37, no. 5, pp. 1178-1191, May 2018, doi: 10.1109/TMI.2018.2792437.